Copyright

by

David Grant Wannlund

2019

**The Thesis Committee for David Grant Wannlund**
**Certifies that this is the approved version of the following Thesis:**

# Imaging the Diffusion of Photoexcited Free Charge Carriers in Organic-Inorganic Trihalide Perovskites

**APPROVED BY**
**SUPERVISING COMMITTEE:**

Keji Lai, Supervisor

Xiaoqin Li

# Imaging the Diffusion of Photoexcited Free Charge Carriers in Organic-Inorganic Trihalide Perovskites

**by**

**David Grant Wannlund**

**Thesis**

Presented to the Faculty of the Graduate School of

The University of Texas at Austin

in Partial Fulfillment

of the Requirements

for the Degree of

**Master of Arts**

**The University of Texas at Austin**

**May 2019**

# Abstract

## Imaging the Diffusion of Photoexcited Free Charge Carriers in Organic-Inorganic Trihalide Perovskites

David Grant Wannlund, M.A.

The University of Texas at Austin, 2019

Supervisor: Keji Lai

Organic-inorganic perovskites have recently attracted significant attention because of their large – and increasing – power conversion efficiencies (PCEs) reaching upwards of 20%. With the promise of application in photovoltaics and optoelectronics, Methylammonium Lead Triiodide ($MAPbI_3$), one such organic-inorganic trihalide perovskite, warrants further investigation of the carrier dynamics at the nanoscale level. After introducing organic-inorganic trihalide perovskites in Chapter 1, I discuss the construction and design challenges of the new Cryochamber Light Assisted Microwave Impedance Microscope (L-MIM) in Chapter 2. In Chapter 3, using the recently constructed Cryochamber L-MIM, I spatially map the intrinsic photoconductivity of $MAPbI_3$ with nanoscale resolution to reveal diffusion lengths below $10\mu m$ independent of the incident laser power density. I demonstrate the utility of L-MIM in revealing nanoscale electronic properties of emerging materials and discuss future applications of this powerful tool in Chapter 4.

# Table of Contents

# List of Figures

# Chapter 1: Introduction

## ORGANIC-INORGANIC TRIHALIDE PEROVSKITES

Organic-Inorganic Trihalide Perovskites with a cubic perovskite structure were first introduced in 1978 when Dieter Weber described $CH_3NH_3PbX_3$ (Methylammonium Lead Triiodide) and remarked at the "intensiven Farbe bemerkenswert [intense remarkable color]" and "elektrischen Leitfähigkeit [electrical conductivity][1]." Although he commented on the optoelectronic properties of these cubic structures, it wasn't until late 2009 that a group from Japan[2] studied these perovskite structures more intensely, kicking off a decade of research into optimizing cubic perovskite structures for applications in solar cells, photodiodes, and lasers[3].

### Crystal Structures of Halide Perovskites

Methylammonium lead triiodide ($CH_3NH_3PbI_3$ or $MAPbI_3$), a cubic perovskite structure, consists of five atoms with an organic methylammonium cation, an inorganic lead cation, and three halide iodide anions. Figure 1.1(a) shows the crystal structure of a cubic perovskite structure with an $ABX_3$ construction[4]. Replacing either of the cations (A or B) or the anion (X) results in drastically different perovskite structures which are classified, using the Goldschmidt tolerance factor, as either orthorhombic, cubic, or hexagonal[5]. The Goldschmidt tolerance factor is given by Equation 1 below where $R_A$ is the radius of cation A, $R_B$ is the radius of cation B, and $R_0$ is the radius of the halide anion. A tolerance level between 0.8 and 1 is favorable for stable cubic perovskite structures[6], providing a useful tool for theorists to foreshadow formable and stable organic-inorganic perovskites.

$$t = \frac{R_A + R_0}{\sqrt{2}(R_B + R_0)}$$ Equation 1

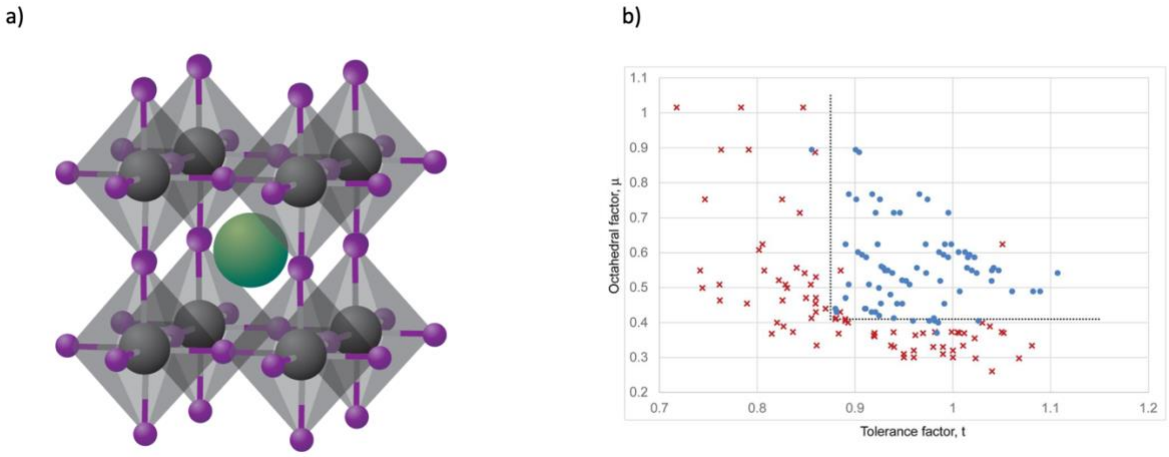


**Figure 1.1** (a) 3D diagram of cubic perovskite structure with $ABX_3$. Adapted from M. Grätzel, Nature Materials, 2014, 13, 838–842. (b) Tolerance factor's role in stable cubic perovskite structures of the form $ABX_3$ where blue (red) points indicate stable (unstable) inorganic perovskites. Adapted from W. Travis, Chem. Sci., 2016, 7, 4548.

### Electronic Characteristics

$MAPbI_3$ is an attractive organic-inorganic trihalide perovskite to study because, in addition to its stable cubic structure, $MAPbI_3$ exhibits promising photovoltaic characteristics and potential for optoelectronic applications. Organic-inorganic trihalide perovskites have large absorption coefficients over a wide swath of visible light

wavelengths and demonstrate low bulk defect densities making them ideal for use in optoelectronic applications and photovoltaics[7].

$MAPbI_3$ has a demonstrated direct band gap energy of $1.6eV$[8] which corresponds to a wavelength toward the infrared side of the visible light spectrum of $774nm$. A band gap energy in this part of the visible light spectrum enables photoexcitation processes at all wavelengths smaller than it – in this case, most all visible light. Figure 1.5(b) illustrates the photoexcitation process where an incident beam with an energy above that of the band gap excites carriers from the valence band to the conduction band. In the conduction band, these carriers contribute to the conductivity but, due to radiative and non-radiative processes, recombine after a lifetime of $\tau$, previously measured to be on the order of $1\mu s$[9]. For a discussion of the power dependence and wavelength dependence of the incident laser on the resulting conductivity in a Transition Metal Dichalcogenide, see Reference 10.

a)

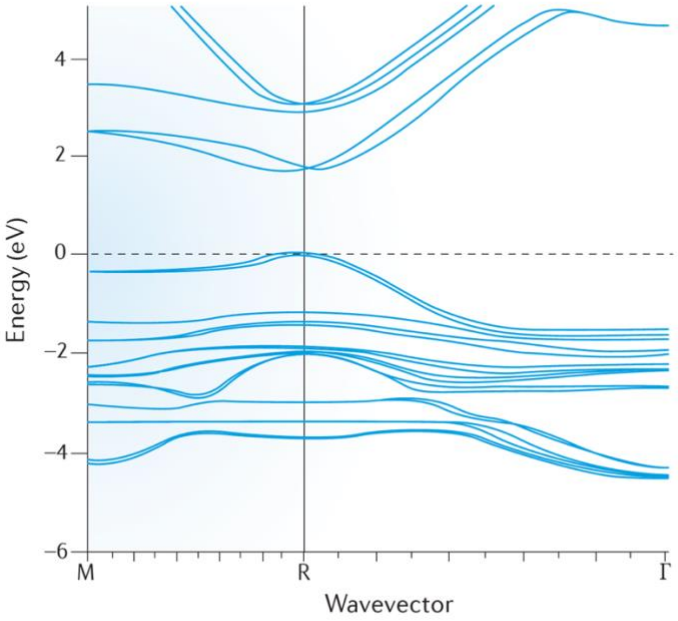


**Figure 1.2** (a) DFT Band gap calculation for $MAPbI_3$ perovskite including spin-orbit coupling effects demonstrating a direct band gap energy of ~1.6eV. Adapted from Brenner et. al., Nature Reviews Materials volume 1, Article number: 15007 (2016).

### Solar Cell Candidates

As a specific example of $MAPbI_3$'s potential optoelectronic applications, they have recently attracted significant attention as potential Photovoltaic (PV) solar cell materials[11,12]. Their low manufacture cost, potential scalability, and ever-increasing power conversion efficiencies (PCEs) have warranted further investigation of the charge

carrier dynamics at the nanoscale level. More importantly, for organic-inorganic perovskites, improvement in these key characteristics has shown no sign of plateauing. Much of the improvement in PCE has occurred over just the past decade, with recent successes achieving PCEs above 20%[13].

Although $MAPbI_3$ is clearly a promising material for photovoltaic and optoelectronic applications, there are still challenges that must be overcome before the material is viable commercially on a large scale. Although, these issues are not truly decoupled, they can generally be separated into two categories: (1) manufacture and scalability[14,15] and (2) transport and electronic characteristics[16,17]. In this report, I focus on the challenges associated with the device transport and electronic characteristics which includes the short sample lifetime before degradation and the sample inhomogeneity induced by grain boundaries and impurities[18]. Using Microwave Impedance Microscopy to study the microscale carrier dynamics in $MAPbI_3$ Perovskites, I improve our ability to create samples with higher PCEs and greater stability.

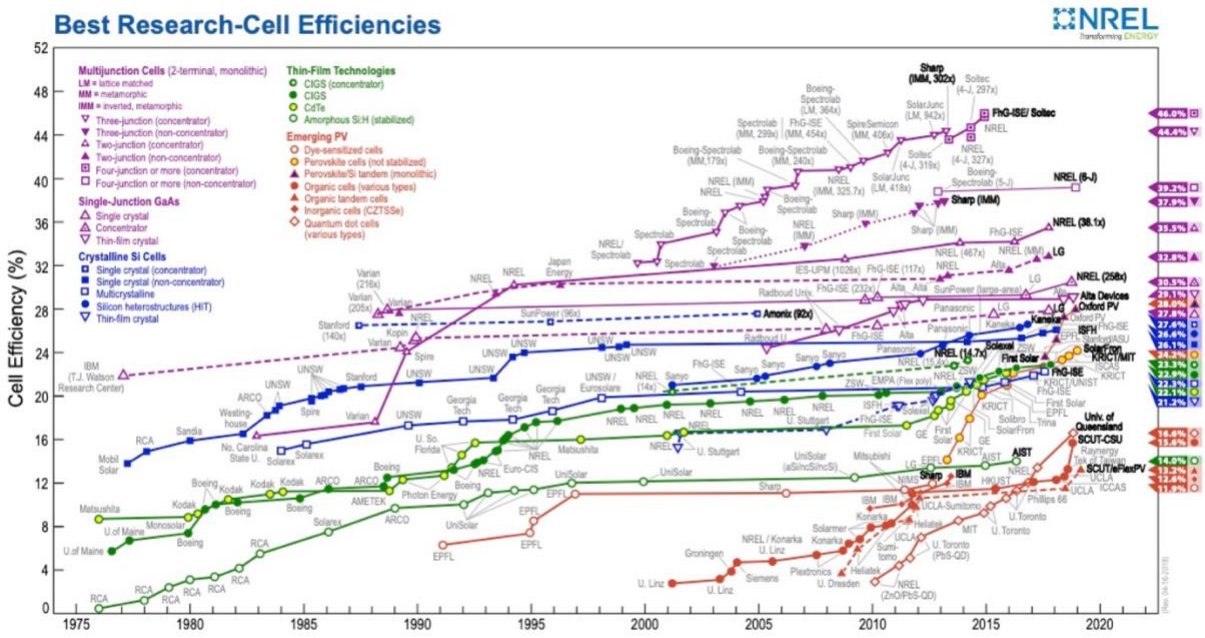


**Figure 1.3** NREL certified solar cell power conversion efficiencies (PCEs). Perovskite solar cells are indicated as emerging PV in red with gold markers. Since emerging on the scene in late 2013, recent certified efficiencies have reached 24.2%. Graph from NREL Best Research-Cell Efficiencies at https://www.nrel.gov/pv/cell-efficiency.html.

### MICROWAVE IMPEDANCE MICROSCOPY

Microwave Impedance Microscopy (MIM) is a Near-Field Scanning Probe Microscopy technique that measures the admittance between a conductive tip ($\sim 100nm$) and a dielectric sample. Developed at Stanford University in 2008 by K. Lai, et. al.[19], MIM is capable of resolutions down to $100nm$ (as limited by the tip diameter), doesn't require the deposition of electrodes, and can be placed on existing Scanning Probe Microscopy setups. An indicator of its utility and versatility, MIM has previously been

used to study the phenomena ranging from topological states in Transition Metal Dichalcogenides[20] to surface acoustic waves in ferroelectrics[21].

**Principles of MIM**

MIM measures the admittance between the tip and the sample to extract the sample conductivity. This process is broken into two parts: (1) the admittance measurement and (2) a Finite Element Analysis (FEA) simulation corresponding the measured admittance with sample conductivity.

Guided by fundamentals in the capacitive interaction between electromagnetic fields and dielectric materials, we measure the admittance between the sample and the tip. The shielding that dielectric materials exhibit in the presence of an external field can be used to non-invasively determine properties of the material. We use a signal generator to create a 1GHz microwave signal and propagate it toward the end of the tip. The microwave signal then interacts with the sample and returns back through the tip to the MIM electronics. This interaction can be described by the complex permittivity, $\epsilon$, where $\epsilon_1$ is the real component of the dielectric constant, $\epsilon_2$ is the imaginary component of the dielectric constant, $\sigma$ is the conductivity, and $\omega$ is the frequency.

$$\epsilon = \epsilon_1 + i(\epsilon_2 + \sigma/\omega) \qquad \text{Equation 2}$$

Once the microwave signal is reflected back through the tip to the electronics, we match the impedance of the tip-sample interaction in order to maximize the reflected signal. This is accomplished by connecting an open-ended cable (of length $\sim\lambda/4$) in parallel with the tip-probe circuit. We must then use the source signal as a reference to cancel background information in the reflected signal. The raw signal is then amplified –

with poor cancellation, the signal will saturate after amplification – and sent to the mixer where the real (MIM-RE) and imaginary (MIM-IM) signals are extracted. MIM-IM and MIM-RE are directly proportional to the imaginary and real parts of the complex permittivity in Eqn. 2. Therefore, since we know MIM-IM/MIM-RE, we know $\epsilon_2$ and $\epsilon_1$ (times some proportionality constant $r$), respectively, as well as the frequency of the source signal, $\omega$. However, in order to determine the conductivity, $\sigma$, we then need to conduct a FEA of the sample, using the known complex permittivity constant for the sample, to determine what conductivity corresponds to the MIM-IM and MIM-RE that we have measured.

$$MIM\text{-}IM = r\epsilon_2 \qquad MIM\text{-}RE = r\epsilon_1 \qquad \text{Equation 3}$$

The FEA is conducted in COMSOL Multiphysics where we define the simulation geometries for the glass substrate, sample material, air, and conducting tip. In order to determine the geometry of the tip, we must scan a calibration sample, often an aluminum dot sample with known conductivity, then conduct another FEA to determine the tip geometry that would yield the measured MIM-IM and MIM-RE given $\sigma_{ALDot}$. Using the FEA simulation, we output the MIM-IM and MIM-RE signals as a function of sample conductivity. Figure 1.4(b) illustrates an example MIM-IM and MIM-RE versus conductivity plot that demonstrates the typical curve for dielectric materials. The MIM-IM signal starts at zero and saturates to a non-zero value while the MIM-RE starts at zero, peaks as MIM-IM increases, then saturates back to zero.

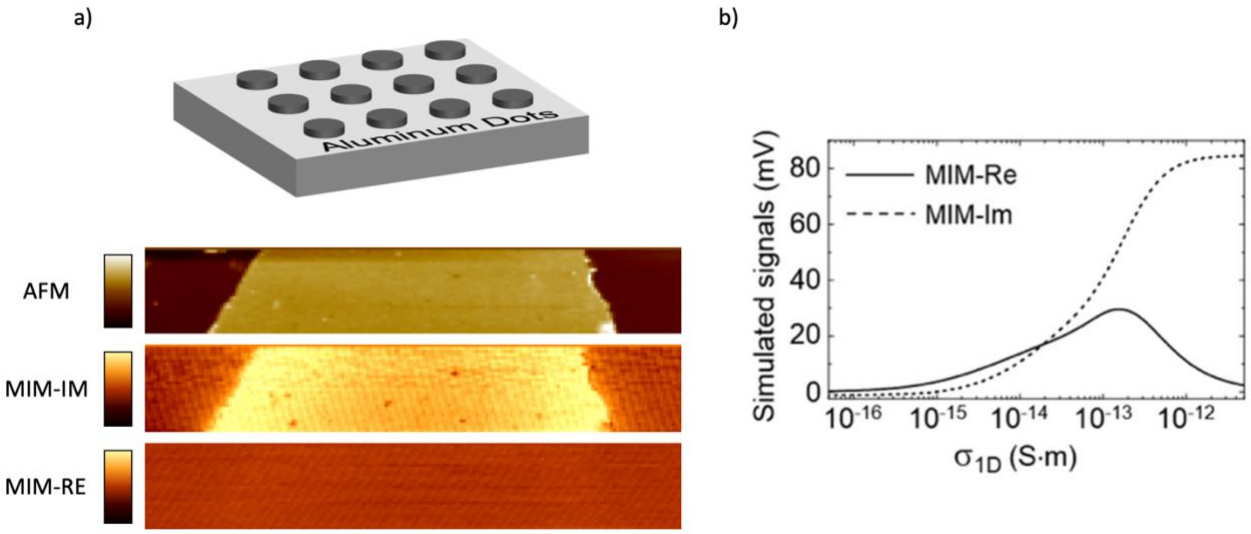


**Figure 1.4** (a) Simplified schematic of aluminum dot sample used to calibrate the MIM and determine the tip geometry as well as AFM, MIM-IM and MIM-RE scans for an aluminum dot sample. Since the aluminum dot is far more conducting than the window of sensitivity for MIM, the imaginary part is bright while there is no signal in the real part. This calibration scan is also used to determine the mixing between the MIM-IM and MIM-RE signals. (b) An example of a simulation curve generated by a FEA in COMSOL Multiphysics to determine the conductivity given measured MIM-IM and MIM-RE signals at the monolayer-bilayer interface of a $WSe_2$ heterostructure. Adapted from Chu, et. al., Nano Lett. 2018, 18, 7200−7206.

After simulating the MIM signals as a function of conductivities, we compare the quotient of the measured MIM signals with the quotient of the simulated MIM signals. This yields Eqn. 5 for the sample conductivity as a function of the quotient between measured MIM-IM and MIM-RE.

$$\frac{MIM\text{-}IM}{MIM\text{-}RE}\Big|_{Sim}(\sigma) = \frac{MIM\text{-}IM}{MIM\text{-}RE}\Big|_{Meas} \qquad f(\sigma) = g \qquad \text{Equation 4}$$

$$\sigma = \frac{MIM\text{-}IM}{MIM\text{-}RE}\Big|_{Meas}\left(\frac{MIM\text{-}IM}{MIM\text{-}RE}\Big|_{Sim}\right) \qquad \sigma = g(f) \qquad \text{Equation 5}$$

Since we are comparing the quotient of the MIM-IM and MIM-RE simulated and measured signals, we need not consider the proportionality constant in Eqn. 3 which describes the relationship between the real and imaginary components of the MIM signal and the corresponding real and imaginary components of the complex permittivity. We do, however, need to consider the implications that this analysis method has on our window of sensitivity. For samples that are very conducting, when the MIM-IM signal is saturated to a positive value and the MIM-RE signal is saturated to zero, the ratio between IM and RE becomes meaningless. There may be no significant difference in the ratio over decades of increase in conductivity. Likewise, if the sample is very insulating, both the MIM-IM and MIM-RE signals saturate to zero, again resulting in a meaningless ratio and meaningless conductivity. In order to move our window of sensitivity, we can introduce additional dielectric layers that encapsulate the sample, moving the effective window of sensitivity from high conductivity lower conductivities. Once included in our FEA simulation, we can extract the conductivity values in the same manner as before. For Van Der Waals materials, this coating is often a thin ($\sim 30nm$) layer of $Al_2O_3$ or a thin layer of hexagonal Boron Nitride (hBN). For perovskite samples, this coating is often a thin layer ($\sim 30nm$) of Polymethyl methacrylate (PMMA) to decrease the effective conductivity of the sample.

**Light Assisted Microwave Impedance Microscopy**

Light Assisted Microwave Impedance Microscopy (L-MIM) introduces an external light source (a laser or coherent white light source) to generate free carriers in a sample allowing us to spatially study free carrier dynamics and, in the future, perhaps other charged quasiparticles such as trions. Previous work using L-MIM by Chu, et. al. has successfully mapped the interfacial trapped charges at heterostructure boundaries[22]. Additionally, Chu has previously demonstrated the significance of L-MIM in analyzing the degradation process and the role of grains and grain boundaries in carrier dynamics in organic-inorganic trihalide perovskites[23].

There are three different scan modes for L-MIM: (1) the tip and laser move together, (2) the laser is stationary while the tip moves, and (3) the tip is stationary while the laser moves. While we have had the capability to conduct scan mode 1, due to design constraints, we are only now beginning to fully realize the potential of scan modes 2 and 3. Scan mode 1 allows us to spatially map intrinsic photoconductivity. Scan modes 2 and 3 allow us to map carrier diffusion in the sample since we can measure the conductivity (and therefore carrier density) at points away from the incident laser.

Photoexcitation is the process through which charge carriers are excited from the valence band to the conduction band after illumination by an external light source. Light Assisted MIM utilizes this physical principle to further study intrinsic material properties such as mobility, carrier lifetime, and diffusion length. Figure 1.5(b) illustrates the process of photoexcitation in greater detail for a $MAPbI_3$ perovskite sample. An incident photon with energy $E = h\nu$ illuminates the sample. If this energy is above the band gap energy (the energy difference between the conduction band minimum and valence band

maximum), then the photon excites the carrier from the valence band to the conduction band. The carrier then remains in the excited state for some period of time, $\tau_{effective}$, before returning to its initial energy state either through recombination or through reemission of a photon[24]. $\tau_{effective}$ can spatially vary in inhomogeneous materials due to differences in trap and defect densities, further illustrating the importance of L-MIM's spatial resolution capabilities.

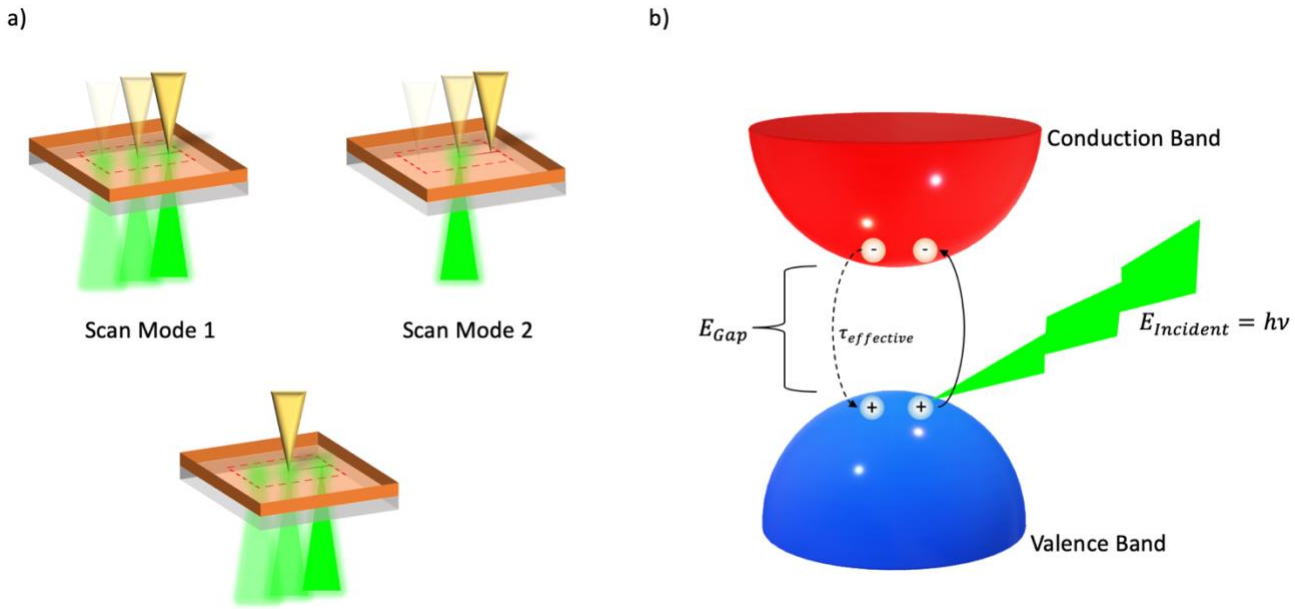


**Figure 1.5** (a) Cartoon illustration of the three different scan modes possible for light assisted microwave impedance microscopy. Scan mode 1 is the mode where the tip and laser are always aligned and move together. Scan mode 2 is the mode where the laser is stationary and the tip moves across the sample. Scan mode 3 is the mode where the tip is stationary and the laser moves across the sample. In all three modes, the sample is stationary. (b) Diagram illustrating the photoexcitation process in $MAPbI_3$ perovskites. Once a carrier is excited to the conduction band by an incident photon, it returns to the valence band after some lifetime, $\tau_{effective}$, due to either recombination or remission of a photon.

Experimentally, the process of conducting Microwave Impedance Microscopy with an introduced external light source becomes a bit more complicated than simply scanning without illumination. In scan mode 1, where the laser and tip are aligned, we first must conduct AFM to find a reference on the sample we can use for alignment. We move the tip to the reference location (as seen on AFM) using software, then move the laser spot to the reference location using an optical CCD image. With a typical laser diameter of 3-5$\mu m$ and a tip diameter on the order of $100nm$, this process regularly results in tip-laser alignment.

In scan mode 2, where instead of aligning the tip and laser we wish to scan the tip around the stationary laser, we need not go through the same alignment process as scan mode 1. Due to differences in experimental setup that will be elaborated on in Chapter 2, a typical laser diameter for scan mode 2 is on the order of 3-6$\mu m$. Once the laser is focused on the sample plane, we simply move the tip such that the scan window covers the area around that laser that we are interested in and conduct the approach for the sample. Additional details regarding the approach process for this setup will follow in Chapter 2.

### CARRIER DIFFUSION IN SEMICONDUCTORS

With the ability to probe conductivity further away from the point of illumination, we must understand the laws that govern carrier diffusion in the steady state solution away from the source laser. Fick's Laws, derived by Adolf Fick in 1885, provide a framework within which to describe the motion of masses (or in this case charges) from

areas of high density to areas of low density[25]. Though Fick's work focused on the diffusion of salt in bodies of water, the same laws govern the motion of carriers when there is an inhomogeneous carrier density throughout a semiconductor. This inhomogeneity could be caused by thermal effects, an external electric field, or an external light source. The diffusion process is an inherently thermally dependent process and at $T = 0K$ there would be no carrier diffusion.

Starting with the charge continuity equation, we can derive the change in current density resulting from free carrier diffusion.

$$\left.\frac{\partial n}{\partial t}\right|_{Total} = \left.\frac{\partial n}{\partial t}\right|_{Drift} + \left.\frac{\partial n}{\partial t}\right|_{Diffusion} + \left.\frac{\partial n}{\partial t}\right|_{Recombination-Generation} + \left.\frac{\partial n}{\partial t}\right|_{External} \quad \text{Equation 6}$$

Then, we can rewrite the drift and diffusion contributions in Eqn. 6 in terms of the change to the current density where q is the charge of a free carrier and $J_N$ is the current density.

$$\left.\frac{\partial n}{\partial t}\right|_{Drift} + \left.\frac{\partial n}{\partial t}\right|_{Diffusion} = \frac{1}{q}\left(\frac{\partial J_{N_x}}{\partial x} + \frac{\partial J_{N_y}}{\partial y} + \frac{\partial J_{N_z}}{\partial z}\right)$$

$$\left.\frac{\partial n}{\partial t}\right|_{Drift} + \left.\frac{\partial n}{\partial t}\right|_{Diffusion} = \frac{1}{q}\vec{\nabla}\cdot\overrightarrow{J_N}$$

Substituting the drift and diffusion terms back into Eqn. 6, we can get,

$$\left.\frac{\partial n}{\partial t}\right|_{Total} = \frac{1}{q}\vec{\nabla}\cdot\overrightarrow{J_N} + \left.\frac{\partial n}{\partial t}\right|_{Recombination-Generation} + \left.\frac{\partial n}{\partial t}\right|_{External}$$

We can further break down the current density into the drift and diffusion components, where $n$ is the local carrier density, $q$ is the carrier charge, $\mu$ is the carrier mobility, $E$ is the applied electric field, and $D_n$ is the Diffusion Constant.

$$\overrightarrow{J_N} = \overrightarrow{J_N}\big|_{Drift} + \overrightarrow{J_N}\big|_{Diffusion} = q\mu nE + qD_n\nabla n$$

At this point, we can make a few simplifications: (1) the change in carrier density resulting from recombination-generation is zero when the system is in a steady state,

$$\frac{\partial n}{\partial t}\Big|_{Recombination-Generation} \rightarrow 0$$

(2) the E field is zero resulting in no contribution from the drift term and (3) the problem can be treated in one dimension. Therefore, the equation for change in carrier density becomes Eqn. 7 where $\varphi$ is the photocarrier generation rate, $\Delta n$ is the spatial difference in carrier density, and $\tau$ is the carrier lifetime.

$$\frac{\partial n}{\partial t}\Big|_{Total} = \frac{1}{q}\nabla^2(qD_n n) + \varphi + \frac{\Delta n}{\tau} \qquad \text{Equation 7}$$

In the steady state solution, we know that the total change in carrier density with respect to time must be zero, which gives us the second order differential equation for the carrier density as a function of position.

$$0 = \frac{1}{q}\nabla^2(qD_n n) + \varphi + \frac{\Delta n}{\tau}$$

We can represent the photocarrier generation rate (where $\eta$ is the IPCE, $P$ is the power density, $h$ is Planck's constant, and $\nu$ is the laser frequency) as

$$\varphi = \frac{\eta P}{h\upsilon}$$

$$0 = \frac{1}{q}\nabla^2(qD_n n) + \frac{\eta P}{h\upsilon} + \frac{\Delta n}{\tau}$$

This equation is a second order differential equation that we can solve for $n$ as a function of position, $x$. The resulting solution is:

$$n_{diffusion}(x) = C_1 e^{-r/L} + C_2 e^{r/L}$$

Since we know that carrier density must go to zero as $r \to \infty$, we can set $C_2 = 0$ resulting in the final solution.

$$n_{diffusion}(r) = C_1 e^{-r/L} \qquad \text{Equation 8}$$

# Chapter 2: Cryochamber Light Assisted Microwave Impedance Microscopy

Cryochamber Light Assisted Microwave Impedance Microscopy is an L-MIM system contained within a low temperature chamber. Our purpose for constructing this new system was two-fold: it enabled two new scan modes (scan modes 2 and 3) to study carrier dynamics away from the point of excitation and also enabled low temperature studies of materials. The design challenges presented by the containment within a small chamber while still incorporating light stimulation and MIM were nontrivial. I will provide an overview of the design process and elaborate on the design challenges encountered.

## DESIGN

The design consists of two main components: (1) a customized Janis ST-500 Optical Suptertran and (2) the MIM component housing, which are both illustrated in Figure 2.1(a) and 2.1(b). The Janis chamber is cooled by liquid helium and contains an optical port on the chamber lid to allow laser stimulation of the sample. Additionally, the chamber consists of two connection interfaces for providing voltages to the piezo stages controlling the tip position and an output for the MIM cable to and from the tip. With a diameter of 3.275in at the top and 2.13in at the bottom, the usable space within the chamber is small in order to minimize helium usage and reduce pump down times.

The MIM component housing, which itself consists of many different elements, must fit within the internal space of the Janis chamber. Included in this housing is the base to secure the setup to the chamber, the legs to elevate the sample holder above the

piezo stages and tip, the mount for the tip, and numerous components for temperature control and thermal coupling. Additionally, there are four piezo stages capable of both DC and AC input: an x stage, y stage, z stage, and positioner stage capable of x, y, and z movement when larger increments are desired. I will focus on the design of the tip mount and the sample holder as these are the two most complicated components of the MIM housing.

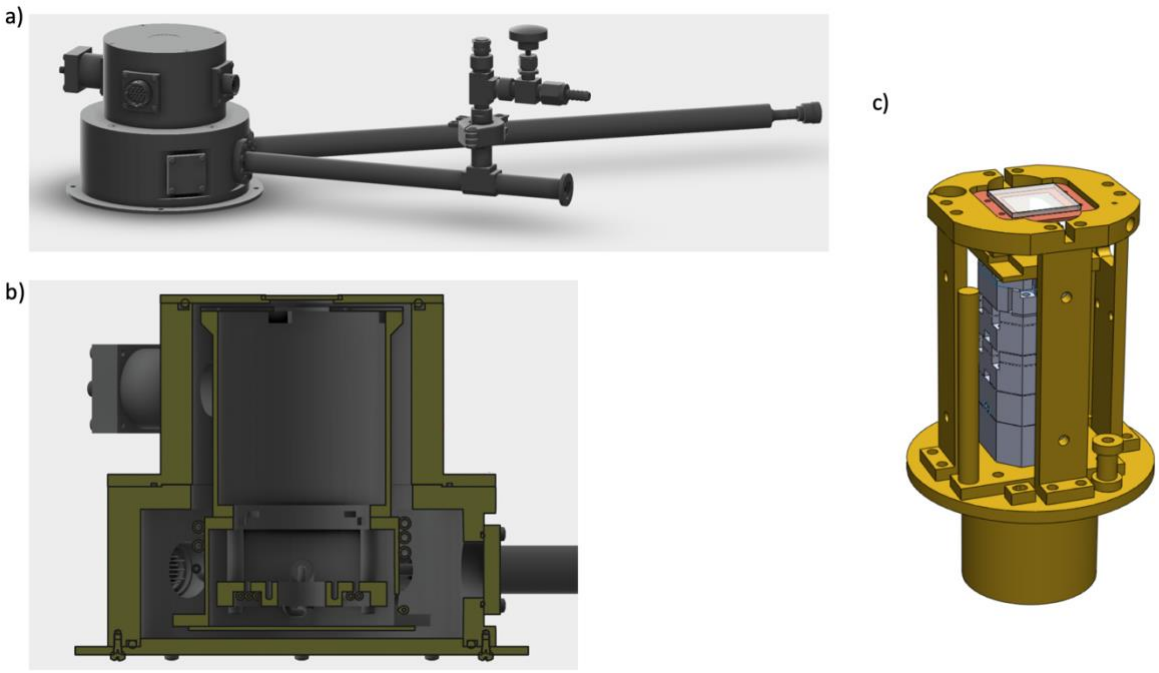


**Figure 2.1** (a) CAD drawing of the customized Janis Supertran cryochamber used in the cryochamber light assisted microwave impedance microscope and (b) a cross section of the internal chamber where the MIM is housed. (c) CAD drawing of the housing for the MIM components.

The tip mount holds the tip and MIM cable that connects to the MIM electronics. Careful thought was had over how to illiminate strain on the piezo stages that may be induced by the externally connected MIM cable. Additionally, since each of the piezo stages (x, y, z, and positioner) can only operate under a certain weight threshold, the tip mount had to be designed with this in mind. The bottom piezo stage is supporting the weight of three additional piezo stages stacked above in addition to the tip mount. Another consideration in the design is the angle of the tip on the tip mount. It had to be large enough that the highest point of the tip assembly was the tip itself while not so large that the tip sample interaction became too weak. The placement of the MIM cable on the mount was also important to consider. The MIM cable had to be close enough to the tip that a wire bond could be made between the two and needed to be flat on the surface of the tip mount. In order to accomplish this, we build a middle section of the tip mount that holds the tip at an angle and cut grooves on each side to support the MIM cable mounting.

The sample holder component holds the sample above the tip and maintains its vertical position by mounting it to the legs connected to the base. Shown in Figure 2.2(b), the sample rests on the top of the holder in an “upside down” position so the top of the sample faces the tip. The laser first hits the back surface of the transparent substrate and is focused on the tip-facing surface of the material. The sample holder also contains a slot for a thermometer, heater, and areas to attach thermal couples to the rest of the apparatus.

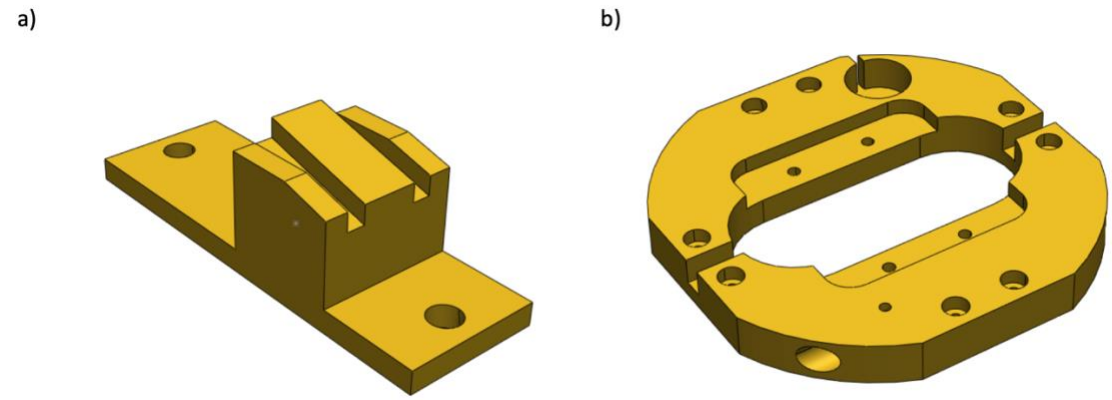


**Figure 2.2** (a) CAD drawing for the tip holder. The notches on the side of the tip mounting ramp allow the microwave cable to be placed close to the tip for easy wirebonding. (b) CAD drawing of the sample mount. The sample sits in the middle upside down so that the surface of the sample is facing the tip beneath it. The laser illuminates the sample from the top of the sample mount. Also shown are notches for temperature regulation.

## EXPERIMENTAL IMPLEMENTATION

### Approaching the Sample

Practically, the approach process for the Cryochamber L-MIM is different from that of a commercial system. Since the Cryochamber L-MIM does not have a feedback system, we must use the principles of MIM to determine when the tip has made contact with the sample. While monitoring the MIM-IM and MIM-RE signals, we use the Z Positioner piezo stage to increase the height of the tip towards the sample. After getting close ($\sim 300 \mu m$) to the sample, we apply an AC signal to the Z piezo stage at the resonant frequency for the equivalent circuit between the tip and sample – this is typically around $350 Hz$ – determined by maximizing the MIM-IM signal and therefore minimizing the MIM-RE signal. We know, at this point, that the MIM-RE signal should be zero, so we use the mixer to further minimize the MIM-RE signal.

Next, we apply a DC input to the Z piezo stage while maintaining the oscillating AC input, to slowly move the tip to the sample surface. As the tip approaches, both MIM signals will increase to a peak value before quickly dropping off to a minimum value. Examples of this approach curve are in Figure 2.3(b). The equivalent circuit that describes the tip-surface interaction reveals why this approach curve occurs. Far away from the surface, as the tip oscillates, there is little change in the capacitance between the tip and sample between the bottom and top points of the oscillation. Since capacitance is inversely related to the separation distance, as the tip moves closer to the sample, the capacitance difference between the top and bottom of the oscillation becomes greater resulting in a peak in MIM signal until the top point of the oscillation is in contact with the sample. Then, as we continue to move the tip up to the sample, the MIM signal drops quickly as the bottom oscillation point of the tip reaches the sample. Not only does this method allow us to determine when the tip has made contact with the sample, but it also allows us to determine the amount of force between the tip and the sample in much the same way that a laser feedback system would allow. Before scanning, the AC modulation on the z stage is turned off and the tip is in stable contact with the sample at a determined force.

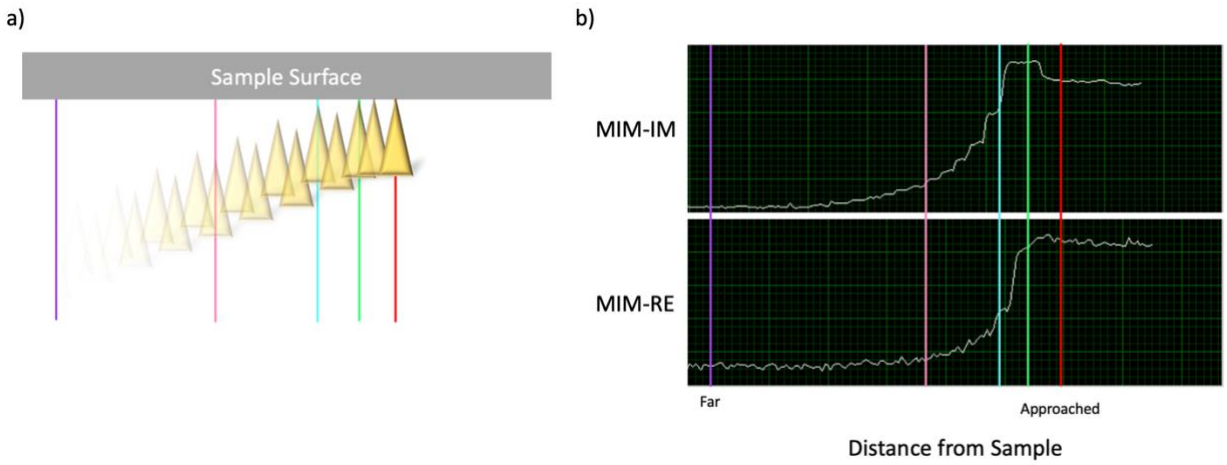


**Figure 2.3** (a) Cartoon illustration of the approach process for the cryochamber light assisted microwave impedance microscope. The tip oscillates at a frequency of approximately 350Hz. As the tip approaches the sample, the MIM channels increase to a maximum value and then decrease. The colored lines correspond to matching periods of time in (b) the MIM signals during the approach.

### SCANNING

With the tip and sample in contact, we raster the tip by applying DC voltage to the x and y piezo stages. However, due to hysteresis that occurs when using piezo stages, after each group of scans we must also scan a reference sample of known size to determine the scan window size. After scanning the reference sample in the Cryochamber L-MIM, we scan it with a properly calibrated AFM to extract the $\mu m/pixel$ ratio to be used in the processing of the raw MIM data.

### FUTURE APPLICATIONS

As of this writing, we have only realized the implications of the new scan modes and have not yet begun low temperature measurements. This will open up a world of new

and exciting physics including exploration of charged quasiparticles and topological states only possible at low temperatures.

Additionally, we have yet to fully explore the possibilities that the new scan modes allow for. Using an Electro-Optic Modulator (EOM) we can conduct time dependent MIM giving us the ability to observe carrier lifetimes in materials. Also, a white light source will allow us to not only sweep incident power density, but also incident wavelength, to spatially map band gap energy in a sample revealing interesting properties at heterostructure interfaces in thin materials.

# Chapter 3: Spatially Resolved Free Carrier Diffusion

## INTRODUCTION

$MAPbI_3$ is an organic inorganic trihalide perovskite that has shown significant promise for application in optoelectronics due to high power conversion efficiencies and high mobilities[3,7,11-13]. Using Light Assisted Microwave Impedance Microscopy, we spatially resolve the changes to photoconductivity in $MAPbI_3$ that result from illuminating the surface with a laser of $\lambda = 517nm$ at power densities ranging from $\sim 10^0\ mW\ cm^{-2}$ to $\sim 10^5\ mW\ cm^{-2}$ in order to investigate the diffusion length of free charge carriers in the perovskite material. With a clearer understanding of carrier dynamics at the nanoscale level, we can, in the future, create cheaper and more efficient perovskite solar cells.

The $100nm$ thick $MAPbI_3$ perovskite samples were prepared by K. Zhu at NREL using the stoichiometry and non-stoichiometry solvent-solvent extraction method[26] to place the perovskite on a glass cover slide. The samples are coated with a thin ($\sim 30nm$) layer of PMMA to encapsulate the sample in order to prevent rapid degradation. Previous work by Chu has demonstrated these particular perovskite samples (as prepared by Kai Zhu at NREL) typically exhibit PCEs ranging from 15% - 18% corresponding to small and large grain sizes, respectively[23].

Shown in Figure 3.1(a), the perovskite sample is illuminated by a chopped laser of wavelength $\lambda = 517nm$ at a frequency of $1kHz$. The laser beam profile can be well-approximated by a Gaussian beam and is focused to a diameter of approximately $5\mu m$ at the perovskite sample surface. We then scan the area around the position of the incident

beam to spatially resolve the sample conductivity. For further discussion of the principles of MIM, refer to Chapter 1.

Figure 3.1(b) also shows the Finite Element Analysis simulation used to determine the sample conductivity given the measured MIM-IM and MIM-RE at each pixel as well as the peak conductivity measured at each incident power density.

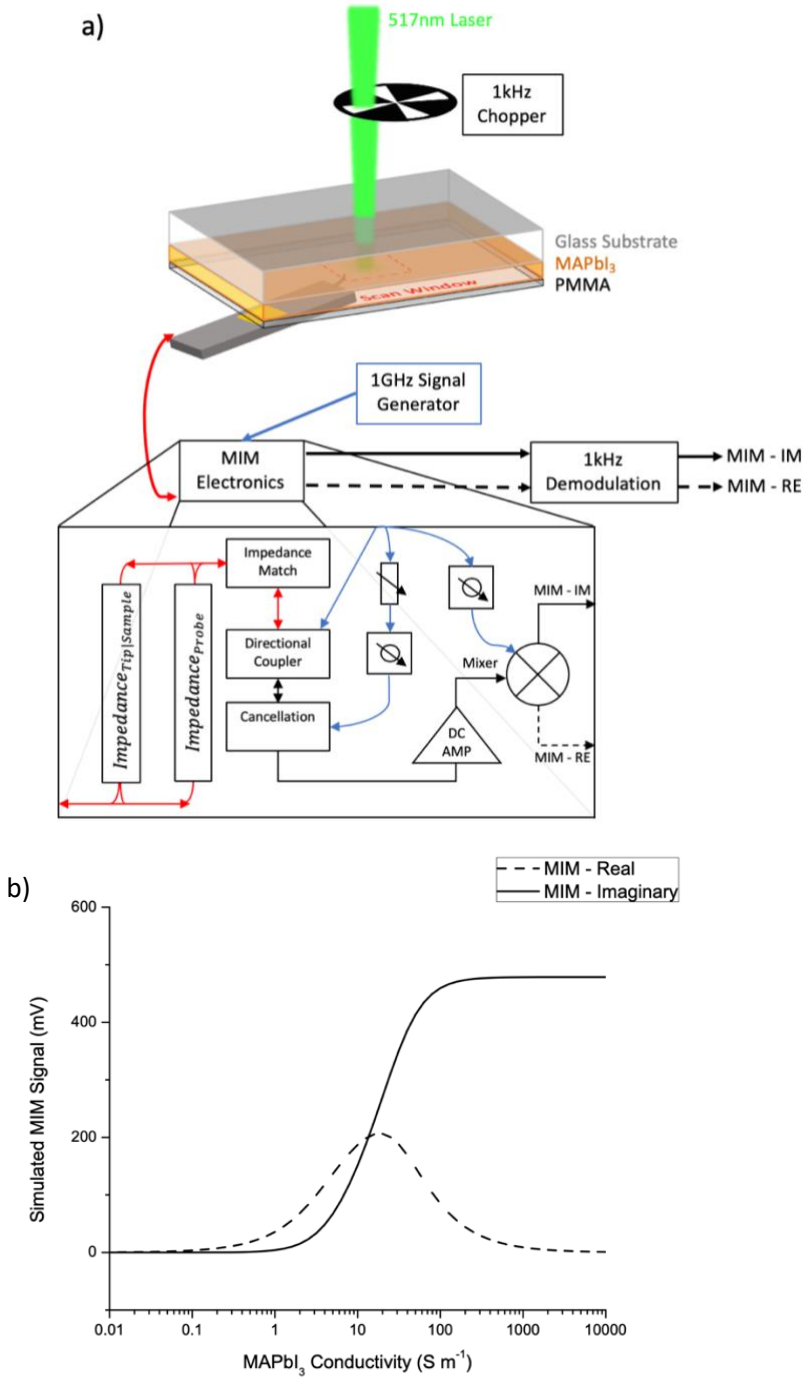


**Figure 3.1** (a) Experimental schematic of L-MIM used to measure conductivity of the $MAPbI_3$ perovskite samples. The stationary laser passes through a 1kHz chopper and then goes to the MIM Electronics where the MIM-IM and MIM-RE are output to then be demodulated by a lock-in amplifier locked at the frequency of the chopper. MIM Electronics details adapted from unpublished manuscript by Y.T. Cui and E.Y. Ma. (b) The simulated MIM signals as a function of $MAPbI_3$ conductivity calculated by FEA using COMSOL Multiphysics.

The mechanical chopper allows us to measure the photoconductivity without the need to create a reference region on the sample surface. Without the chopper, it would be necessary to scratch a portion of the sample away to reveal the glass substrate. With the chopper, we demodulate both the MIM-IM and MIM-RE signals using a lock-in amplifier and output the $Laser_{ON} - Laser_{OFF}$ signals. We are effectively using the $Laser_{OFF}$ signal as our reference which removes the need to create a reference surface on the sample. Figure 3.2(b) illustrates measured MIM signals with a chopper used to create a reference on $MAPbI_3$. As expected, with the laser off and chopper on, the MIM signals are both zero because there is no difference between the laser on and our reference: laser off.

Figure 3.2(a) also shows the topography information for the $MAPbI_3$ samples. The smaller grain size of these samples is consistent with those that Z. Chu studied with a PCE of $\sim 15\%$[23]. Additionally, the sample is topographically uniform as indicated by AFM, but not electronically uniform as indicated by the MIM-IM and MIM-RE images. Due to the onset of moisture-induced degradation, the photoconductivity becomes spatially inhomogeneous, which we account for in the later sections of the analysis.

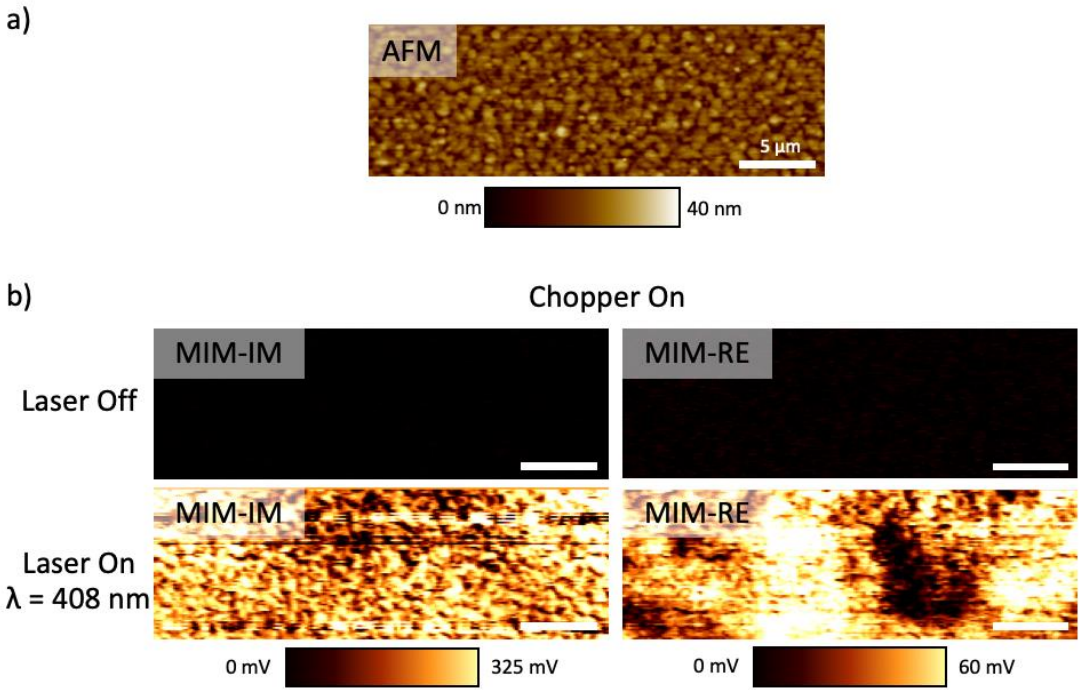


**Figure 3.2** (a) AFM image of the $MAPbI_3$ perovskite surface coated in PMMA indicating a small grain boundary size. (b) MIM images for an above gap energy laser with a 1kHz chopper. As expected, with the chopper on and the laser off, there is no difference between our reference (laser off) and the laser on so there is no signal in the MIM channels.

## RESULTS

With the aim to study the diffusion length of $MAPbI_3$ perovskites, we measure the conductivity while keeping the incident beam stationary and scanning the tip. Figure 3.3(a) shows the MIM-IM and MIM-RE images over increasing power density at a constant wavelength of $\lambda = 517nm$ and Figure 3.3(b) shows the calculated conductivity images. Without any illumination we do not see any signal in the MIM channels due to the chopper. As the incident power density increases, the MIM-IM signal at the center of the beam spot continues to increase while the MIM-RE signal at the center of the beam

spot increases to $\sim 170mV$ and then decreases again at high incident power densities. This matches the simulated curve in Figure 3.1(b) as the MIM-RE signal increases to about $\sim 200mV$ at its peak.

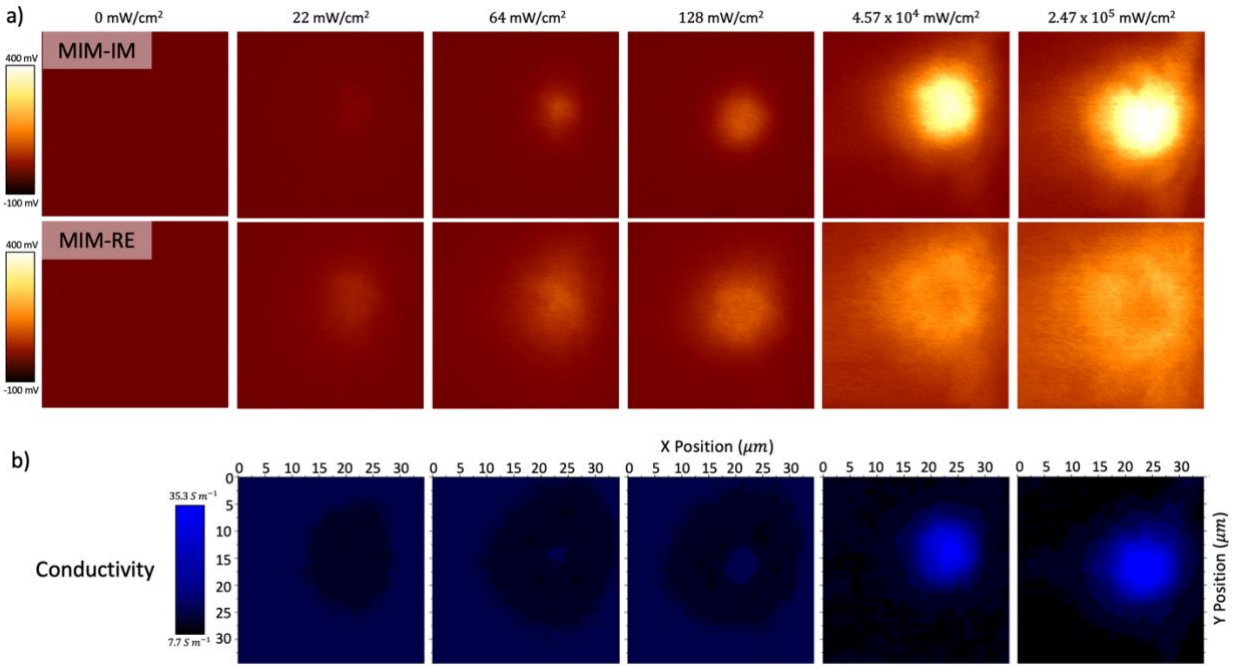


**Figure 3.3** (a) MIM Images of the free carrier diffusion from the incident point of a 517nm laser with a width, $w_0 = 2.64\mu m$, at increasing power densities. In the first image the laser is off and both the real and imaginary signals are zero because there is no photoexcitation. As the incident power density increases, the real and imaginary signals both increase until the real part plateaus and begins to decrease between $\sim 10^3\ mW\ cm^{-2}$ and $\sim 10^4\ mW\ cm^{-2}$, while the imaginary part continues to increase. (b) Using the FEA simulation, the conductivity images are calculated. The images are shown with a log-scale color bar. Values far away from the incident laser point should be discounted because the contrast between MIM-IM and MIM-RE is negligible meaning there is a large uncertainty in the calculated conductivity value.

A line profile of through the center of the conductivity reveals the conductivity as a function of position from the center of the incident beam. The conductivity can be described as $\sigma = en\mu_e$ This is then converted to a normalized carrier density as a function of position since $n \propto \sigma$.

In order to determine the diffusion length, we compare the measured normalized carrier density to the simulated normalized carrier density given the incident beam width, $w_0$, and diffusion length, $L$. This simulation is a Finite Element Analysis where we break the $x$-$y$ position space into a grid consisting of $0.1\mu m^2$ elements each filled with a delta function of the number of incident carriers present due to the incident beam (where the $n(r) = e^{-2r^2/w_0}$). Since the carrier lifetime is on the order of $ns$ and the chopper operates on the order of $ms$, we can treat the diffusion with the steady state solution derived in Chapter 1 where the subscript $x, y$ indicates the finite element position.

$$n_{x,y_{diffusion}}(r) = C_{x,y_1} e^{-r/L} \qquad \text{Equation 9}$$

With the recognition that the total number of carriers must be conserved in the steady state solution, we calculate the constant, $C_{x,y_1} = N_{x,y_{Inc}}/2\pi r$ where $N_{x,y_{Inc}}$ is the number of incident carriers in element $x, y$. For each element, we calculate the diffused carriers at every element a distance $r$ away from the central element, including the carriers that remain in the central element at $r = 0$. We then sum the number of diffused carriers at every element to numerically calculate the spatially diffused carrier density resulting from an incident beam of width $w_0$ and a material with diffusion length $L_D =$

$\sqrt{D\tau}$. The diffusion constant, $D$, is taken to be homogenous spatially throughout the material and independent of the power density of the incident beam. Figure 3.4(a) shows the simplified schematic for the carrier diffusion simulation with a $0.1\mu m$ by $0.1\mu m$ grid. Figure 3.4(b) plots a comparison between the gaussian incident beam profile, the summed diffusion simulation curve, and an example element diffusion curve at (x = 0,y = 0). The final summed diffusion curve is the sum of all 346x346 diffusion element curves.

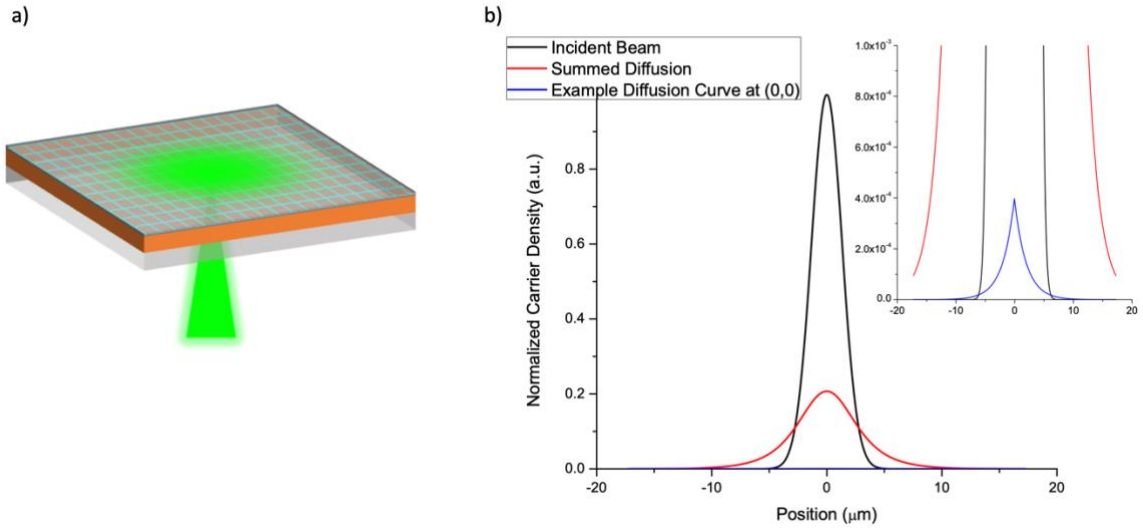


**Figure 3.4** (a) A schematic of the FEA simulation to calculate the diffusion curve in $MAPbI_3$. The sample is broken into a $0.1\mu m$ by $0.1\mu m$ grid where the gaussian profile of the incident beam determines the initial number of carriers in each quantized "box." (b) Incident beam curve shown with the calculated diffusion curve for $w_0 = 2.6$ and $L_d = 2\mu m$. The inset of the graph shows one calculated diffusion curve element for the element at ($x = 0, y = 0$). There are 346x346 diffusion elements (blue) that all contribute to the summed diffusion curve (red).

Figure 3.5(b) shows the profile cuts of the measured normalized carrier density compared to multiple simulated diffusion length profiles. Of note is the large variation in the measured carrier density profile. This is likely the result of the inhomogeneous conductivity illustrated by the MIM images in Figure 3.2(b) and leads to non-centrosymmetric profiles of the measured carrier density. We fit a range of diffusion length curves to show the maximum and minimum diffusion length that contain the measured carrier density, yielding the uncertainty in the diffusion length.

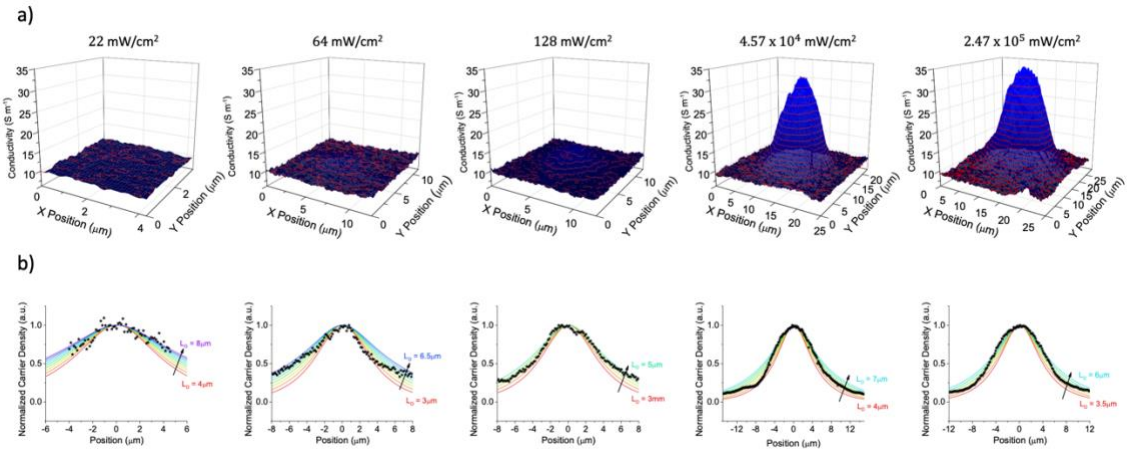


**Figure 3.5** (a) 3D conductivity plots for each incident power density zoomed in to the region of incident illumination. (b) Line cuts through the center of the conductivity plots with a range of simulated diffusion length curves plotted for comparison.

After comparing the multiple diffusion length curves to the measured carrier density, the diffusion length and the uncertainty for each incident power density is displayed in Figure 3.5(b). The uncertainty in diffusion length was determined by plotting all diffusion length curves that contain the data and the diffusion length is the curve that best fits the majority of the data. The uncertainty in the diffusion length at each power density is large because of the asymmetry in the measured carrier density curve. Over this range of power densities, there is no clear power dependence in the diffusion length of $MAPbI_3$. However, additional measurements in other power regimes may reveal a nonlinear trend in the diffusion length as has been reported by other groups[27].

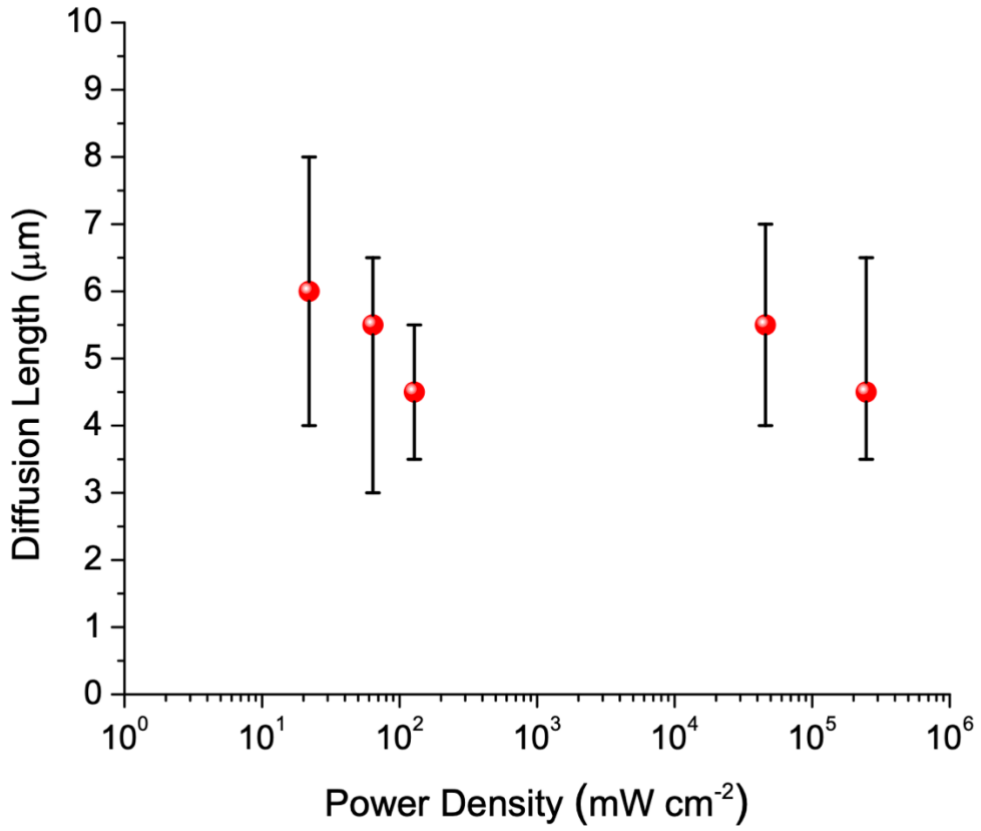


**Figure 3.6**: Diffusion Length as a function of power density for $MAPbI_3$ perovskite. There is no clear power dependence, however more measurements in different power regimes may reveal different trends. The large uncertainties are a result of the asymmetry in the carrier density curves that the simulated diffusion curves are fit to.

After comparing the simulated diffusion curves to the measured carrier density curves, the diffusion length of this $MAPbI_3$ sample varies from $L_d = 4.5\mu m$ to $L_d = 6\mu m$ with an uncertainty range of $\sigma_{Low} = 2.5\mu m$ to $\sigma_{High} = 8\mu m$. This is in reasonable agreement with groups that have previously reported diffusion lengths in $MAPbI_3$ on the order of $10\mu m$[28].

# Chapter 4: Discussion and Future Work

With nanoscale resolution and the ability to measure intrinsic conductivity without the need for electrodes, MIM is a noninvasive tool that can spatially map material properties to reveal the underlying physics that drives them. Additionally, the new cryochamber L-MIM will provide opportunities to reveal exciting new physics by probing at low temperatures and with new scan modes.

We have already begun to utilize the new scan modes of the cryochamber L-MIM by measuring the diffusion length of an organic-inorganic trihalide perovskite, $MAPbI_3$. By spatially resolving the conductivity after illumination by an above band gap laser, we can spatially resolve the carrier density, and therefore map the diffusion of free carriers. After performing a FEA simulation of the diffusion process and comparing it to the measured carrier density versus position, we have preliminarily determined that the diffusion length in $MAPbI_3$ is not strongly correlated to incident power density over the power regime measured and ranges from $L_d = 4.5\mu m$ to $L_d = 6\mu m$. However, further measurements at both lower and higher power densities are required to determine if this trend holds in other power regimes. The large uncertainty in the diffusion length at each incident power density results from the asymmetry observed in many of the carrier density line cuts. This could be caused either by air exposure degradation as the sample was scanned or by illumination-enhanced degradation[29]. More data will be needed to eliminate this asymmetry and reduce the uncertainty in the measured diffusion length.

In the future, it will be possible to spatially probe many phenomena only observable at low temperatures as we prepare the new cryochamber L-MIM. We will also

expand our capabilities to the time domain with the addition of an Electro-optical Modulator (EOM) which will allow us to probe carrier lifetimes on the nanosecond timescale. The addition of a xenon lamp white light source will also expand our capabilities with respect to energy mapping as we remove the discretization limit imposed by select wavelength laser diodes.

Light Assisted Microwave Impedance Microscopy has already proven to be a useful tool for probing carrier dynamics in materials ranging from TMDs such as $WSe_2$ to organic-inorganic perovskites such as $MAPbI_3$. As new materials are developed and new MIM capabilities are achieved, MIM will continue to prove its usefulness in understanding the underlying physics of emerging materials.

# References


[1] Weber, D. (1978). CH 3 NH 3 PbX 3 , ein Pb(II)-System mit kubischer Perowskitstruktur, *1445*(August), 1443–1445.

[2] A. Kojima, K. Teshima, Y. Shirai, & T. Miyasaka. (2009). Organometal Halide Perovskites as Visible-Light Sensitizers for Photovoltaic Cells. *Journal of the American Chemical Society*, *131*(17), 6050–6051.

[3] Xing, G., Mathews, N., Lim, S. S., Yantara, N., Liu, X., Sabba, D., … Sum, T. C. (2014). Low-temperature solution-processed wavelength-tunable perovskites for lasing. *Nature Materials*, *13*(5), 476–480.

[4] Grätzel, M. (2014). The light and shade of perovskite solar cells. *Nature Materials*, *13*(9), 838–842.

[5] Travis, W., Glover, E. N. K., Bronstein, H., Scanlon, D. O., & Palgrave, R. G. (2016). On the application of the tolerance factor to inorganic and hybrid halide perovskites: A revised system. *Chemical Science*, *7*(7), 4548–4556.

[6] *Ibid*.

[7] Hao, F., Stoumpos, C. C., Cao, D. H., Chang, R. P. H., & Kanatzidis, M. G. (2014). Lead-free solid-state organic-inorganic halide perovskite solar cells. *Nature Photonics*, *8*(6), 489–494.

[8] Brenner, T. M., Egger, D. A., Kronik, L., Hodes, G., & Cahen, D. (2016). Hybrid organic - Inorganic perovskites: Low-cost semiconductors with intriguing charge-transport properties. *Nature Reviews Materials*, *1*(1).

[9] Shi, D., Adinolfi, V., Comin, R., Yuan, M., Alarousu, E., Buin, A., … Bakr, O. M. (2015). Low Trap-State Density and Long Carrier Diffusion in Organolead Trihalide Perovskite Single Crystals. *Science*, *347*(6221), 519–522.

[10] Chu, Z., Han, A., Lei, C., Lopatin, S., Li, P., Wannlund, D., … Lai, K. (2018). Energy-Resolved Photoconductivity Mapping in a Monolayer-Bilayer WSe 2 Lateral Heterostructure. *Nano Letters*.

[11] Stranks, S. D., & Snaith, H. J. (2015). Metal-halide perovskites for photovoltaic and light-emitting devices. *Nature Nanotechnology*, *10*(5), 391–402.

[12] Grancini, G., Marras, S., Prato, M., Giannini, C., Quarti, C., De Angelis, F., … Petrozza, A. (2014). The impact of the crystallization processes on the structural and optical properties of hybrid perovskite films for photovoltaics. *Journal of Physical Chemistry Letters*, *5*(21), 3836–3842.

[13] Li, J., Jiu, T., Duan, C., Wang, Y., Zhang, H., Jian, H., … Li, Y. (2018). Improved electron transport in MAPbI3 perovskite solar cells based on dual doping graphdiyne. *Nano Energy*, *46*(December 2017), 331–337.

[14] Shao, Y., Wang, Q., Dong, Q., Yuan, Y., & Huang, J. (2015). Vacuum-free laminated top electrode with conductive tapes for scalable manufacturing of efficient perovskite solar cells. *Nano Energy*, *16*, 47–53.

[15] Rocks, C., Svrcek, V., Maguire, P., & Mariotti, D. (2017). Understanding surface chemistry during MAPbI3 spray deposition and its effect on photovoltaic performance. *Journal of Materials Chemistry C*, *5*(4), 902–916.

[16] Sendner, M., Nayak, P. K., Egger, D. A., Beck, S., Müller, C., Epding, B., … Lovrinčić, R. (2016). Optical phonons in methylammonium lead halide perovskites and implications for charge transport. *Materials Horizons*, *3*(6), 613–620.

[17] Colella, S., Mosconi, E., Fedeli, P., Listorti, A., Gazza, F., Orlandi, F., … Mosca, R. (2013). MAPbI 3-x Cl x mixed halide perovskite for hybrid solar cells: The role of chloride as dopant on the transport and structural properties. *Chemistry of Materials*, *25*(22), 4613–4618.

[18] Chu, Z., Yang, M., Schulz, P., Wu, D., Ma, X., Seifert, E., … Lai, K. (2017). Impact of grain boundaries on efficiency and stability of organic-inorganic trihalide perovskites. *Nature Communications*, *8*(1), 1–8.

[19] Lai, K., Kundhikanjana, W., Kelly, M., & Shen, Z. X. (2008). Modeling and characterization of a cantilever-based near-field scanning microwave impedance microscope. *Review of Scientific Instruments*, *79*(6).

[20] Shi, Y., Kahn, J., Niu, B., Fei, Z., Sun, B., Cai, X., … Cui, Y. T. (2019). Imaging quantum spin Hall edges in monolayer WTe2. *Science Advances*, *5*(2), 1–7.

[21] Wu, X., Petralanda, U., Zheng, L., Ren, Y., Hu, R., Cheong, S.-W., … Lai, K. (2017). Low-energy structural dynamics of ferroelectric domain walls in hexagonal rare-earth manganites. *Science Advances*, *3*(5), e1602371.

[22] Chu, Z., Han, A., Lei, C., Lopatin, S., Li, P., Wannlund, D., … Lai, K. (2018). Energy-Resolved Photoconductivity Mapping in a Monolayer-Bilayer WSe2 Lateral Heterostructure. *Nano Letters*.

[23] Chu, Z., Yang, M., Schulz, P., Wu, D., Ma, X., Seifert, E., … Lai, K. (2017). Impact of grain boundaries on efficiency and stability of organic-inorganic trihalide perovskites. *Nature Communications*, *8*(1), 1–8.

[24] Brenner, T. M., Egger, D. A., Kronik, L., Hodes, G., & Cahen, D. (2016). Hybrid organic - Inorganic perovskites: Low-cost semiconductors with intriguing charge-transport properties. *Nature Reviews Materials*, *1*(1).

[25] Lowney, J. R., & Larrabee, R. D. (1980). The Use of Fick's Law in Modeling Diffusion. *IEEE Transactions on Electron Devices*, (2), 2–5.

[26] Yang, M., Zhou, Y., Zeng, Y., Jiang, C. S., Padture, N. P., & Zhu, K. (2015). Square-Centimeter Solution-Processed Planar CH3NH3PbI3 Perovskite Solar Cells with Efficiency Exceeding 15%. *Advanced Materials*, *27*(41), 6363–6370.

[27] Wanyi, N., Hsinhan, T., Reza, A., Blancon, J.-C., Amanda, J. N., Guatam, G., & Jared, J. C. (2015). High-efficiency solution-processed perovskite solar cells with millimeter-scale grains. *Science*, *347*(6221), 522–525.

[28] Shi, D., Adinolfi, V., Comin, R., Yuan, M., Alarousu, E., Buin, A., … Bakr, O. M. (2015). Low trap-state density and long carrier diffusion in organolead trihalide perovskite single crystals. *Science*, *347*(6221), 519–522.

[29] Abdelmageed, G., Jewell, L., Hellier, K., Seymour, L., Luo, B., Bridges, F., … Carter, S. (2016). Mechanisms for light induced degradation in MAPbI3 perovskite thin films and solar cells. *Applied Physics Letters*, *109*(23).